

Masses of the components of SB2 binaries observed with *Gaia*. V. Accurate SB2 orbits for 10 binaries and masses of the components of 5 binaries. ^{**} ††

J.-L. Halbwachs^{1†}, F. Kiefer^{2,3}, Y. Lebreton^{3,4}, H.M.J. Boffin⁵, F. Arenou⁶,
J.-B. Le Bouquin⁷, B. Famaey¹, D. Pourbaix⁸, P. Guillout¹, J.-B. Salomon⁹,
and T. Mazeh¹⁰

¹ *Université de Strasbourg, CNRS, Observatoire astronomique de Strasbourg, UMR 7550, 11 rue de l'Université, F-67000 Strasbourg, France*

² *Institut d'Astrophysique de Paris, CNRS/UMR7095, 98bis boulevard Arago, F-75014 Paris, France*

³ *LESIA, Observatoire de Paris, PSL Research University, CNRS, Sorbonne Université, UPMC Univ. Paris 06, Univ. Paris Diderot, Sorbonne Paris Cité, F-92195 Meudon, France*

⁴ *Univ Rennes, CNRS, IPR (Institut de Physique de Rennes) - UMR 6251, F-35000 Rennes, France*

⁵ *European Southern Observatory, Karl-Schwarzschild-Strasse 2, D-85748 Garching bei München, Germany*

⁶ *GEPI, Observatoire de Paris, PSL Research University, CNRS, Université Paris Diderot, Sorbonne Paris Cité, Place Jules Janssen, F-92195 Meudon, France*

⁷ *Univ. Grenoble-Alpes, CNRS, IPAG, 38000 Grenoble, France*

⁸ *FNRS, Institut d'Astronomie et d'Astrophysique, Université Libre de Bruxelles, boulevard du Triomphe, 1050 Bruxelles, Belgium*

⁹ *Institut UTINAM, CNRS UMR6213, Université Bourgogne Franche-Comté, OSU THETA, Observatoire de Besançon, BP 1615, F-25010 Besançon Cedex, France*

¹⁰ *School of Physics and Astronomy, Tel Aviv University, Tel Aviv 69978, Israel*

Accepted . Received 2019 ; in original form 2019

ABSTRACT

Double-lined spectroscopic binaries (SB2s) are one of the main sources of stellar masses, as additional observations are only needed to give the inclinations of the orbital planes in order to obtain the individual masses of the components. For this reason, we are observing a selection of SB2s using the SOPHIE spectrograph at the Haute-Provence observatory in order to precisely determine their orbital elements. Our objective is to finally obtain masses with an accuracy of the order of one percent by combining our radial velocity (RV) measurements and the astrometric measurements that will come from the *Gaia* satellite. We present here the RVs and the re-determined orbits of 10 SB2s. In order to verify the masses we will derive from *Gaia*, we obtained interferometric measurements of the ESO VLTI for one of these SB2s. Adding the interferometric or speckle measurements already published by us or by others for 4 other stars, we finally obtain the masses of the components of 5 binary stars, with masses ranging from 0.51 to 2.2 solar masses, including main-sequence dwarfs and some more evolved stars whose location in the HR diagram has been estimated.

Key words: binaries: spectroscopic, stars: fundamental parameters, stars: individual: HIP 104987

1 INTRODUCTION

Estimating the mass of stars is a fundamental step in understanding the internal processes that determine how stars

work, how bright they shine, and for how long. When the mass is known with sufficient precision, modelling not only enlightens us on the physical processes it depicts (e.g. Claret & Torres 2019), but also provides constraints on parameters that are not directly accessible, such as age and helium content (e.g. Lebreton 2005).

It is only possible to obtain a mass for a few very specific stars, but these are the basis of calibration relationships that allow the masses of other stars to be estimated from

* based on observations performed at the Observatoire de Haute-Provence (CNRS), France

† based on data obtained with the ESO Very Large Telescope under programme 094.D-0624 and 097.D-0688.

‡ E-mail: jean-louis.halbwachs@astro.unistra.fr

more accessible data, such as spectral type, color indices or absolute luminosity (e.g. Eker et al. 2015; Moya et al. 2018; Mann et al. 2019). These calibrations paved the way for population synthesis models, ultimately allowing to estimate the stellar mass-to-light ratios of galaxies from their observed colours or spectral energy distributions (e.g. Bell & de Jong 2001), which are central to the estimate of their dark matter content (e.g. Lelli et al. 2016).

There are only a limited number of direct methods for measuring the mass of a star, and they all apply to components of double stars. Most (but not all) use the double-lined spectroscopic binaries (SB2s), for which the orbital elements allow to calculate a minimum value of the mass of each component, $M \sin^3 i$, where i is the inclination of the orbit. This parameter can be obtained from the following complementary techniques:

- The eclipsing binaries (EBs) have historically been considered the Royal Road of stellar astrophysics, and this reputation has not been denied. When they are also double-lined spectroscopic binaries (SB2s), photometric and spectroscopic observations make it possible to deduce not only the masses of the components, but also their radii, their effective temperatures (e.g. Torres et al. 2019), and even the distance of the system with sufficient precision to test trigonometric parallaxes obtained by astrometric satellites (Munari et al. 2004). Unfortunately, a binary can present eclipses only if its orbital plane is close to the line of sight. This makes the EBs quite rare among binaries, and introduces a bias in favour of short-period systems. As a result, the components of many EBs are affected by the presence of the companion, and only a minority of EBs are representative of single stars.

- Visual binaries (VBs) are another case where stellar masses can be obtained, when they are also SB2s. Formerly confined to the domain of long periods, they have moved into the domain of moderate periods (from a few weeks to decades) thanks to the development of interferometry, whether speckle (e.g. McAlister 1996; Balega et al. 2007) or long-baseline (see e.g. Le Bouquin et al. 2011). The results are even better for EB, VB and SB2 systems combined (e.g. Lester et al. 2019; Gallenne et al. 2019). However, the number of short period VB systems is still limited by the considerable resources required to observe an orbit, by the brightness required to observe a star and by the low luminosity contrast between the two components.

- Astrometric binaries (ABs). We call here “astrometric binaries” unresolved double stars whose photocentre describes a measurable orbit, such as the 235 orbits observed by the “HIGH Precision PARallax COLlecting Satellite” (Hipparcos, ESA 1997). The masses of the AB components may be derived when the system is also a VB (Martin & Mignard 1998), or an SB2 (Jancart et al. 2005). The masses thus obtained have an accuracy of a few percent, at the best. However, much more precise masses should be obtained in the near future, thanks to astrometric measurements from the Gaia satellite.

Compilations of the most accurate masses has been given by Torres, Andersen & Giménez (2010), and in the references mentioned above about the calibrations.

This paper is the fifth in a series dedicated to the determination of precise masses using the *Gaia* satel-

lite (Gaia collaboration 2016). Although the Gaia collaboration has already published two Data Releases (Gaia collaboration 2016b, 2018), precise masses can only be calculated when the full data transits are available, with the full release for the nominal mission, according to the Gaia web site¹.

The first paper of the series (Halbwachs et al. 2014, Paper I hereafter) presented the selection of about 70 SB2s for which the masses of the components could be precisely calculated by combining the astrometric transits of the *Gaia* satellite with precise radial velocity (RV) measurements obtained using the “Spectrographe pour l’Observation des PHénomènes des Intérieurs Stellaires et des Exoplanètes” (SOPHIE, Perruchot et al. 2008) at the Haute-Provence Observatory. The selection included about fifty known SB2s, and about twenty SB1s that our first spectroscopic observations had transformed into SB2s by detecting the secondary component.

Simultaneously with the spectroscopic observations, we obtained interferometric observations for five stars of our selection. These observations were carried out with the auxiliary telescopes of the ESO Very Large Telescope with the “Precision Integrated-Optics Near-infrared Imaging Experiment” (PIONIER) instrument. In the second paper (Halbwachs et al. 2015, Paper II hereafter), they were already used to derive preliminary masses for the components of two SB2s, using published RV measurements completed with a few ones that we had obtained from a preliminary reduction of our SOPHIE observations. We have thus demonstrated the possibility of using these measurements to validate the masses that we will later obtain from *Gaia*.

In the third and in the fourth paper, (Kiefer et al. 2016, 2018, Paper III and Paper IV, respectively), we presented the RV measurements and the revised SB2 orbits of 10 and 14 binaries, respectively. Out of a total of 24 SB2s revised orbits, we found four for which an interferometric orbit had already been published. By combining the interferometric measurements of these stars with our RV measurements, we have calculated the masses of the components of these four binaries (one in Paper III and three in Paper IV).

The present paper is particularly in line with the latter two, since we apply the same methods to treat 10 more SB2s. Five of these binary stars were resolved by long-base or speckle interferometry: One was found in the Fourth Catalog of Interferometric Measurements of Binary Stars² (INT4 hereafter; Third catalogue: Hartkopf et al. 2001), one was observed by Balega et al. (2007), and three have been observed for us with the PIONIER instrument attached to ESO’s Very Large Telescope Interferometer. The interferometric orbits of two of the latter were derived in Paper II, but the third is calculated here for the first time. Thus, we give here the masses of the components of the five binaries.

The article is organized as follows: the observations are presented in Section 2; this section includes the spectroscopic observations of 10 SB2s, but also the interferometric observations of one of these stars. The derivation of the RVs is in Section 3. The elements of the spectroscopic orbits are

¹ <https://www.cosmos.esa.int/web/gaia/release>

² <https://www.usno.navy.mil/USNO/astrometry/optical-IR-prod/wds/int4>

Table 1. The SB2s analyzed in this paper.

Name	Alt. name	V	Period ^a	N_{spec} ^b	Span ^c	SNR ^d
HIP	HD/BD	(mag.)	(day)		(period)	
<i>Previously published SB2</i>						
HIP 20601	HD 27935	8.93	156	16	14	50
HIP 73449	HD 132756	7.31	2529	11	0.88	97
HIP 76006	HD 138525	6.39	582	12	4.6	142
HIP 77725	BD +11 2874	9.36	1016	13	1.9	53
HIP 96656	HD 186922	8.04	4347	14	1.0	102
HIP 104987	HD 202447/8	3.93	99	14	12	371
HIP 117186	HD 222995	7.11	86	14	26	96
<i>SB2s identified in Paper I, previously published as SB1s</i>						
HIP 7134	HD 9313	7.81	53.5	16	50	98
HIP 61732	BD +17 2512	9.18	595	11	4.3	46
HIP 101452	HD 196133	6.70	88	11	30	129

^a The period values are taken from our solutions.

^b N_{spec} gives the number of spectra collected with SOPHIE and taken into account in the derivation of the orbital elements.

^c Span is the total time span of the observation epochs used in the orbit derivation, counted in number of periods.

^d SNR is the median signal-to-noise ratio of all the SOPHIE spectra of a given star at 5550 Å.

derived in Section 4. The masses of the components of 5 binaries separated by interferometry are derived in Section 5, where we briefly discuss the evolutionary state of these stars and their positions in the HR diagram. Section 6 is the conclusion.

2 OBSERVATIONS

2.1 Spectroscopic observations

As before, the observations were performed at the T193 telescope of the Haute-Provence Observatory, with the SOPHIE spectrograph. From 2010 to 2016, they were carried out in visitor mode by assigning priorities to the stars based on ephemerides. Since semester 2014B, we have regularly obtained observations in service mode that we request for selected dates in order to complete phase coverage while avoiding blends that would give unusable RV measurements. Exceptions to this rule are generally stars for which the preliminary orbit was inaccurate, or stars suspected for a time of being multiple systems.

The list of stars treated in this article is given in Table 1, where the number of usable spectra and the number of cycles covered by the observations are indicated. A minimum of 11 usable spectra was requested in order to calculate orbital elements with reliable uncertainties.

The exposure times have been adapted to the observation conditions in order to have a signal-to-noise ratio (SNR) appropriate for each star. The SNR is a compromise between the need to have sufficiently smooth spectra to distinguish the components, and the need to have exposure times shorter than one hour, which is the limit in service mode.

The spectra are used to derive the RVs of the components, as explained in Section 3 hereafter.

2.2 Interferometric measurements

We obtained additional interferometric observations for one of the 10 SB2s, namely HIP 104987. This star was observed with the four 1.8 m Auxiliary Telescopes of ESO VLTI, using the PIONIER instrument (Berger et al. 2010; Le Bouquin et al. 2011) in the H-band. Twelve set of observations were made, all resulting in the separation of the components. A first set of observations were done in Visitor Mode under Prog. ID 094.D-0624(A-F) on the nights of 6, 8, 17, 18, and 31 October 2014 for a total of 106 data points. The baseline was A1-G1-K0-J3. In addition, data were obtained in Service Mode, under Prog. ID 097.D-0688(A), on 7 epochs between 29 May 2016 and 25 August 2018. Each time 2 sets of observations were obtained, leading to a total of 70 data points. The baseline was A0-G1-J2-J3.

The observations were reduced with the PNDRS package presented by Le Bouquin et al. (2011). For each epoch, the visibilities and closure phases were fitted to a binary model to determine the relative separation between the components, ρ , the position angle of the secondary component with respect to the primary, θ , and the flux ratio in the H band. The binary model is non-linear, and χ^2 minimization can lead to several local minima. Therefore, a classical gridding approach is used to locate the deepest minimum in parameter space. A Levenberg-Marquardt algorithm is then used to derive the best-fitting parameters and the covariance matrix, from which are extracted the following parameters of the astrometric error ellipsoid: the semi-major axis, σ_a , the semi-minor axis, σ_b , and the position angle of the semi-major axis, θ_a ; by construction, θ_a is between 0 and 180°. These parameters are presented in Section 5.5, where they are used to calculate the visual orbit of HIP 104987, then the masses of the components.

3 RADIAL VELOCITY MEASUREMENTS

3.1 Choice of spectroscopic templates

Reliable RV measurements first require the choice of spectroscopic templates. As for the mask used in ordinary 1D-cross correlation function (1D-CCF), the choice of templates with a set of absorption lines as similar as possible to the actual absorption lines in the observed spectrum is crucial to the estimation of velocities, and to the value of the resulting masses. This is even more important in the present case, when the observed spectrum is the combination of two different components with different or similar sets of absorption lines. For that reason, the choice of the stellar parameters that characterise a spectrum was carefully optimised as explained hereafter.

Before any further analysis, the SOPHIE multi-order spectra are reduced, flattened and normalised as explained hereafter: The spectra are deblazed, flattened, and the pseudo-continuum are normalized using a p -percentile filter (Hodgson et al. 1985). The χ^2 of the residuals of the prepared observed spectrum fitted by the sum of two similarly prepared model atmosphere templates from the PHOENIX database (Huber et al. 2011) is minimised with respect to T_{eff} , $\log g$, $[\text{Fe}/\text{H}]$, $v \sin i$ and flux ratio $\alpha = F_B/F_A$ at 4916 Å. Order 33 around the Ca I line at 6120 Å was mainly used, but early type stars,

Table 2. The stellar parameters of the 10 SB2s, determined from the PHOENIX library by χ^2 optimization around the Ca I line at 6121 Å. Sun’s parameters derived with the same protocol are given in the last row.

HIP/Name	$^a T_{\text{eff},1}$ $T_{\text{eff},2}$ (K)	$^b \log g_1$ $\log g_2$ (dex)	$V_1 \sin i_1$ $V_2 \sin i_2$ (km s $^{-1}$)	$^c [\text{Fe}/\text{H}]$ (dex)	α (flux ratio)	N_{spec}	Spectral orders Median wavelength (Å)
HIP 7134	4754 ± 48	3.75 ± 0.12	4.2 ± 0.7	-0.31 ± 0.04	0.045 ± 0.005	4	33
	5057 ± 243	5.13 ± 0.18	0 (fixed)				6142
HIP 20601	5628 ± 67	4.55 ± 0.07	3.4 ± 1.1	-0.17 ± 0.05	0.105 ± 0.004	4	33
	4847 ± 83	5.18 ± 0.10	1.1 ± 0.7				6142
HIP 61732	6021 ± 16	4.44 ± 0.00 $_{MS}$	5.8 ± 0.1	0.16 ± 0.05	0.115 ± 0.009	2	24, 33
	5070 ± 326	4.59 ± 0.06 $_{MS}$	3.0 ± 0.8				5293, 6142
HIP 73449	5500 ± 110	4.42 ± 0.08	3.8 ± 0.3	-0.39 ± 0.10	0.781 ± 0.115	4	33
	5400 ± 71	4.47 ± 0.07	4.7 ± 0.9				6142
HIP 76006	6314 ± 26	4.10 ± 0.04	8.8 ± 1.1	-0.03 ± 0.04	0.157 ± 0.034	4	24, 33
	6083 ± 152	4.72 ± 0.14	4.7 ± 0.4				5293, 6142
HIP 77725	4378 ± 60	5.49 ± 0.05	2.7 ± 0.6	-0.11 ± 0.04	0.972 ± 0.051	3	33
	4323 ± 29	5.45 ± 0.07	3.2 ± 0.9				6142
HIP 96656	5128 ± 8	4.58 $_{MS}$	3.2 ± 0.5	-0.37 ± 0.06	0.486 ± 0.033	2	33
	4876 ± 36	4.63 $_{MS}$	3.8 ± 0.1				6142
HIP 101452	9767 ± 288	3.08 ± 0.10	21.7 ± 0.1	0.08 ± 0.06	0.254 ± 0.075	4	24, 33
	7915 ± 552	3.24 ± 0.13	32.2 ± 2.1				5293, 6142
HIP 104987	5111 ± 7	3.08 ± 0.11	5.1 ± 0.1	-0.09 ± 0.01	0.814 ± 0.032	4	24, 33
	7488 ± 223	3.87 ± 0.15	23.3 ± 5.9				5293, 6142
HIP 117186	6208 ± 138	3.05 ± 0.17	42.1 ± 1.4	-0.70 ± 0.02	0.347 ± 0.008	4	24, 33
	5785 ± 110	3.27 ± 0.19	13.2 ± 0.4				5293, 6142
Sun	5836 ± 40	4.58 ± 0.10	4.9 ± 0.2	-0.12 ± 0.04		4	33
						4	6142

^aMinimum systematic uncertainties on T_{eff} are about 100 K.

^bThe MS subscript indicates that the $\log g$ did not converge to a realistic value (> 5) and was fixed to be on the Main Sequence following $\log g = 12 - 2 \log T_{\text{eff}}$ (Angelov 1996).

^cGiven the systematic error on $[\text{Fe}/\text{H}]_{\text{sun}}$, a more reliable value of uncertainty on $[\text{Fe}/\text{H}]$ should be at least 0.1 dex.

such as HIP 61732 A, HIP 76006 A&B, HIP 101452 A&B, HIP 104987 B and HIP 117186 A, required the additional use of order 24, bluer and with deep and more numerous lines than on the red wing of their spectrum. When possible and for each binary, the stellar parameters were optimised for up to four observed spectra with the largest RV separation between the two components of the binary. In some case, the recursive algorithm leads to unreasonably low or high $\log g$. In those case, main sequence relation of $\log g$ with T_{eff} is assumed. The results of this preliminary step are presented in Table 2. As in paper IV, this table also gives the results of our method applied to the Sun, using Ceres and Vesta spectra. Since we measured the Sun metallicity to be of -0.12 dex, this could be considered as the realistic minimum uncertainty on the metallicities that we derived.

It should be noted that, since the minimisation of the parameters is obtained by a recursive algorithm, the resulting parameters are not full-proof against systematics, because metallicity $[\text{Fe}/\text{H}]$ and effective temperature T_{eff} can be degenerate on ranges of order ± 400 K and ± 0.5 dex, especially when $v \sin i$ strongly departs from 0. The derivation of the Sun’s parameters using spectra observed with SOPHIE on Ceres and Vesta (see Table 2) shows that the effective temperature and surface gravity are correctly derived within 100 K and 0.1 dex but the metallicity is underestimated by 0.12 dex. Nevertheless, the derived model templates are the best-matching with respect to the observed spectra and lead

to the best precision possible for RV derivation of the two binary components, as explained below.

3.2 Derivation of the RVs using TODMOR

After the templates have been fixed, the RVs of the components are derived using TODMOR, which is the multi-order version of the Two-Dimensional Cross-Correlation algorithm TODCOR (Zucker & Mazeh 1994; Zucker et al. 2004). TODMOR consists in cross-correlating the observed spectra with the sum of two templates each shifted with independent values of Doppler shift. All orders of the spectra are taken into account, except the few red orders with strong telluric absorptions. This leads to a direct measurement of each SB2 component radial velocities from the location of the 2D-CCF peak position.

The RV uncertainties are given by the Hessian of the CCF peak, as explained in Zucker et al. (2004). These uncertainties are intrinsic to the observed spectrum and do not reflect instrument systematics or Earth atmospheric turbulence effects. Therefore, they are generally underestimated.

The resulting RVs and uncertainties are in Table 3. The orbital elements are calculated by correcting these misestimated uncertainties, as described in Section 4 below.

Table 3. New radial velocities from SOPHIE and obtained with TODMOR. The uncertainties must still be corrected as explained in Section 4. Outliers are marked with an asterisk (*) and are not taken into account in the analysis.

HIP 7134							HIP 20601						
BJD	RV_1	σ_{RV1}	RV_2	σ_{RV2}	$O_1 - C_1$	$O_2 - C_2$	BJD	RV_1	σ_{RV1}	RV_2	σ_{RV2}	$O_1 - C_1$	$O_2 - C_2$
-2400000	km s ⁻¹	km s ⁻¹	km s ⁻¹	km s ⁻¹	km s ⁻¹	km s ⁻¹	-2400000	km s ⁻¹	km s ⁻¹	km s ⁻¹	km s ⁻¹	km s ⁻¹	km s ⁻¹
55440.5885	10.4191	0.0065	-50.632	0.121	-0.0194	-0.124	55532.4785	25.7705	0.0230	63.225	0.138	-0.0101	0.156
55783.5935*	-16.9886*	0.0069*	-111.655*	0.198*	0.0930*	-99.780*	55965.3794*	42.9021*	0.0117*	38.7895*	0.0621*	-0.0277*	-1.1649*
55864.3935	-8.4295	0.0077	-24.316	0.121	0.0082	-0.307	56243.5140	46.9362	0.0114	34.3063	0.0689	0.0042	-0.2538
55933.2411	-1.2729	0.0097	-33.669	0.156	0.0215	0.368	56323.2404	-24.3260	0.0115	130.6220	0.0686	-0.0038	0.0230
56148.5790	-3.2947	0.0062	-31.1841	0.0985	0.0051	0.0375	56323.3136	-24.7308	0.0112	131.0056	0.0656	0.0106	-0.1584
56243.3345	10.5423	0.0068	-50.504	0.119	0.0156	0.127	56323.3628	-24.9478	0.0114	131.4262	0.0680	0.0058	-0.0239
56323.2640	-23.1077	0.0071	-3.531	0.114	0.0039	-0.121	56323.4538	-25.1850	0.0128	131.7206	0.0742	-0.0028	-0.0375
56525.5388	-6.8886	0.0066	-25.907	0.110	0.0076	0.266	56323.5101	-25.2270	0.0147	131.7337	0.0825	-0.0191	-0.0592
56526.5927	-8.4490	0.0067	-24.296	0.103	-0.0009	-0.301	56324.2438	-16.4954	0.0113	119.9919	0.0675	-0.0059	-0.0500
56618.4321	10.9971	0.0073	-51.473	0.131	0.0001	-0.182	56324.4318	-12.1233	0.0123	114.2045	0.0712	-0.0008	0.0487
56889.5888	9.1280	0.0071	-48.721	0.120	-0.0035	-0.049	56324.4718	-11.1305	0.0128	113.0198	0.0742	0.0114	0.1856
57414.2895	-22.0863	0.0102	-4.597	0.156	-0.0121	0.269	56619.5265	33.7580	0.0139	52.5084	0.0877	-0.0049	0.1986
57664.4175	-27.4393	0.0070	2.693	0.111	-0.0103	0.042	57009.4242	48.1266	0.0107	32.8635	0.0644	0.0088	-0.0982
57668.6030	-32.5635	0.0069	9.693	0.120	-0.0061	-0.157	57295.6072	49.3997	0.0117	31.3802	0.0681	-0.0030	0.1503
57967.5713	-2.6955	0.0067	-31.913	0.106	-0.0187	0.183	57729.4798	-10.4057	0.0084	111.8797	0.0533	0.0002	0.0376
58049.5126	-38.0529	0.0070	17.613	0.120	0.0070	0.038	57734.4367	30.0813	0.0093	57.3817	0.0587	0.0010	0.1084
58104.3403	-38.0874	0.0075	17.640	0.129	0.0045	0.021	57744.4419	47.8803	0.0104	33.1556	0.0577	-0.0076	-0.1161

HIP 61732							HIP 73449						
BJD	RV_1	σ_{RV1}	RV_2	σ_{RV2}	$O_1 - C_1$	$O_2 - C_2$	BJD	RV_1	σ_{RV1}	RV_2	σ_{RV2}	$O_1 - C_1$	$O_2 - C_2$
-2400000	km s ⁻¹	km s ⁻¹	km s ⁻¹	km s ⁻¹	km s ⁻¹	km s ⁻¹	-2400000	km s ⁻¹	km s ⁻¹	km s ⁻¹	km s ⁻¹	km s ⁻¹	km s ⁻¹
55306.4207	-8.3478	0.0145	-26.6353	0.0463	-0.0958	0.2674	55692.4882	-0.7934	0.0309	17.0707	0.0370	-0.0356	-0.0534
55605.5921	-23.0190	0.0224	-5.6286	0.0735	-0.0384	0.3460	55784.3889	0.4684	0.0133	15.8849	0.0161	-0.0086	0.0049
55933.6824	-6.3513	0.0785	-29.404	0.238	-0.0083	0.211	56033.5122	4.2001	0.0141	12.5914	0.0162	0.2753	0.1855
55965.6664	-5.4211	0.0213	-30.4971	0.0680	0.0130	0.4097	56324.5998*	8.1433*	0.0150*	8.1301*	0.0211*	0.4223*	-0.4506*
56324.4596*	5.5374*	0.0495*	12.427*	0.132*	23.7667*	25.153*	56414.4664*	8.1472*	0.0140*	8.1379*	0.0198*	-0.6900*	0.6818*
56700.6136	-22.9432	0.0199	-5.6340	0.0631	-0.0161	0.4167	56764.5111	12.9019	0.0135	3.1792	0.0159	-0.0959	-0.0845
56764.4370	-23.6411	0.0208	-4.7600	0.0680	0.0085	0.2643	57073.6441	16.3382	0.0149	-0.0219	0.0123	0.0428	0.0372
57073.5168	-9.4719	0.0179	-24.8731	0.0589	-0.0082	0.3079	57159.4899	16.9948	0.0128	-0.7958	0.0154	-0.0239	-0.0080
57159.4472	-5.4137	0.0193	-30.4919	0.0616	0.0451	0.3797	57505.5554	15.5184	0.0127	0.6945	0.0154	-0.0165	-0.0127
57786.6697	-7.6073	0.0315	-27.2952	0.0966	0.0131	0.5049	57786.7050	1.5771	0.0169	14.7238	0.0204	-0.0281	-0.0194
57790.6406	-8.1229	0.0251	-26.6537	0.0787	0.0416	0.3734	57819.6003	0.2040	0.0124	16.1244	0.0151	-0.0205	-0.0099
57882.3660	-22.3616	0.0218	-6.3860	0.0710	0.0608	0.3820	57884.3865	-1.6977	0.0128	17.9910	0.0156	-0.0519	-0.0280
							57907.4966	-2.0944	0.0128	18.4137	0.0155	-0.0384	-0.0186

HIP 76006							HIP 77725						
BJD	RV_1	σ_{RV1}	RV_2	σ_{RV2}	$O_1 - C_1$	$O_2 - C_2$	BJD	RV_1	σ_{RV1}	RV_2	σ_{RV2}	$O_1 - C_1$	$O_2 - C_2$
-2400000	km s ⁻¹	km s ⁻¹	km s ⁻¹	km s ⁻¹	km s ⁻¹	km s ⁻¹	-2400000	km s ⁻¹	km s ⁻¹	km s ⁻¹	km s ⁻¹	km s ⁻¹	km s ⁻¹
55306.5029	-42.8153	0.0110	-52.7052	0.0222	-0.0892	-0.2235	56033.5344	5.4237	0.0469	-6.3398	0.0489	0.0317	-0.1054
55605.6601	-59.5963	0.0144	-32.1284	0.0343	-0.0035	-0.0147	56324.6204	-3.0082	0.0328	2.4322	0.0302	0.0543	0.1727
55693.4977*	-47.8939*	0.0128*	-55.4821*	0.0361*	2.3308*	-12.0557*	56413.5956	-4.1716	0.0305	3.4173	0.0279	0.0630	-0.0196
56033.5161	-39.9011	0.0141	-56.1313	0.0397	-0.0180	-0.2164	56414.4882	-4.1921	0.0300	3.4314	0.0270	0.0518	-0.0150
56148.3668	-67.1434	0.0144	-22.8255	0.0346	0.0040	0.1652	56525.3487	-5.1084	0.0291	4.1920	0.0326	-0.0903	-0.0322
56324.5920*	-47.6020*	0.0144*	-46.8863*	0.0402*	0.0042*	-0.2977*	56890.3385	6.2889	0.0341	-7.1557	0.0314	0.0230	-0.0434
56414.4732*	-46.7105*	0.0130*	-39.0619*	0.0372*	-2.4072*	11.5151*	57073.6786	4.2096	0.0231	-5.1364	0.0249	-0.1544	0.0652
56526.3470	-41.2841	0.0134	-53.7254	0.0333	0.0682	0.4151	57160.4459	1.4910	0.0265	-1.9056	0.0229	0.3734	0.0345
56763.6293	-60.6714	0.0151	-30.7782	0.0364	0.0160	0.0136	57505.5763	-4.9516	0.0320	3.9906	0.0348	-0.0967	-0.0695
57073.6520	-42.0726	0.0108	-52.9364	0.0234	0.0988	0.2150	57602.3763	-5.1568	0.0276	4.2329	0.0301	-0.0990	-0.0312
57159.4946	-40.3507	0.0130	-55.2787	0.0371	-0.0292	0.1067	57883.4782	4.4851	0.0274	-5.4379	0.0294	-0.1273	0.0134
57884.3934	-65.0381	0.0155	-25.4839	0.0367	0.0120	0.0396	57915.4439	6.8188	0.0259	-7.7011	0.0281	0.0002	-0.0336
57886.5146	-65.9159	0.0126	-24.3583	0.0302	0.0054	0.1130	57967.3789	8.3892	0.0291	-9.2368	0.0264	-0.0259	0.0348
57908.4167	-64.9054	0.0138	-25.6758	0.0330	0.0081	0.0125							
57967.3659	-54.7292	0.0134	-38.7045	0.0381	-0.0725	-0.6301							

4 DERIVATION OF THE SPECTROSCOPIC ORBITS

The SB2 orbits are calculated by fitting SB models with a Levenberg–Marquardt algorithm, thanks to the routines in Press et al. (1996). However, it is necessary to operate

in several steps in order to correct the uncertainties in the RVs. The uncertainties of the RVs derived above are unreliable, which will lead to two types of error: first, the weights are inversely proportional to the squares of the uncertainties, and the RVs of one component could be overweighted

Table 3. Continued.

HIP 96656							HIP 101452						
BJD	RV_1	σ_{RV1}	RV_2	σ_{RV2}	$O_1 - C_1$	$O_2 - C_2$	BJD	RV_1	σ_{RV1}	RV_2	σ_{RV2}	$O_1 - C_1$	$O_2 - C_2$
-2400000	km s ⁻¹	km s ⁻¹	km s ⁻¹	km s ⁻¹	km s ⁻¹	km s ⁻¹	-2400000	km s ⁻¹	km s ⁻¹	km s ⁻¹	km s ⁻¹	km s ⁻¹	km s ⁻¹
54036.2377	-9.0509	0.0085	3.0741	0.0188	-0.0029	-0.0740	55440.4261	16.939	0.211	-42.368	0.703	0.040	0.704
54242.5740	-9.8948	0.0073	4.0682	0.0157	-0.0029	-0.0055	55784.4621*	-6.452*	0.147*	-10.195*	0.920*	-0.838*	0.273*
54382.3061	-10.0356	0.0081	4.2243	0.0171	-0.0034	-0.0033	56034.6277	-33.121	0.143	29.949	0.577	0.016	0.557
54609.5475	-9.7375	0.0077	3.9465	0.0172	0.0052	0.0364	56147.4640	14.544	0.151	-40.641	0.519	-0.057	-0.898
56414.5879	0.7110	0.0074	-7.4156	0.0165	0.0174	0.1214	56243.2835	9.778	0.152	-32.584	0.811	-0.000	0.176
56525.3890	1.4861	0.0076	-8.3370	0.0172	0.0003	0.0689	57159.5702*	-14.830*	0.148*	-1.19*	1.05*	-0.135*	-3.88*
56619.4076	2.1267	0.0084	-9.1430	0.0185	-0.0134	-0.0193	57160.5648*	-15.627*	0.146*	-1.383*	0.683*	-0.078*	-5.302*
56890.4790	3.8014	0.0080	-11.0163	0.0173	-0.0001	-0.0705	57295.3811	9.8731	0.0925	-31.602	0.533	0.0335	1.247
57159.5549	4.6588	0.0079	-11.8947	0.0167	-0.0001	-0.0084	57602.4958	-18.898	0.134	7.997	0.565	-0.063	-0.682
57295.3366	4.5014	0.0077	-11.7592	0.0166	-0.0042	-0.0409	57633.4364	16.725	0.135	-43.591	0.599	-0.018	-0.744
57505.6141	3.1099	0.0124	-10.2134	0.0269	0.0125	-0.0398	57884.5573	-53.615	0.134	60.043	0.600	0.015	0.974
57602.4588	1.9160	0.0081	-8.8603	0.0185	-0.0070	0.0252	57967.4676	-41.757	0.134	41.743	0.717	0.090	-0.262
58302.5008	-8.4244	0.0076	2.4612	0.0170	0.0085	-0.0123	57969.4488	-47.624	0.139	50.173	0.579	-0.082	-0.079
58351.4943	-8.8211	0.0076	2.9015	0.0168	-0.0070	0.0100	58058.3569	-51.095	0.140	54.538	0.551	-0.005	-0.854

HIP 104987							HIP 117186						
BJD	RV_1	σ_{RV1}	RV_2	σ_{RV2}	$O_1 - C_1$	$O_2 - C_2$	BJD	RV_1	σ_{RV1}	RV_2	σ_{RV2}	$O_1 - C_1$	$O_2 - C_2$
-2400000	km s ⁻¹	km s ⁻¹	km s ⁻¹	km s ⁻¹	km s ⁻¹	km s ⁻¹	-2400000	km s ⁻¹	km s ⁻¹	km s ⁻¹	km s ⁻¹	km s ⁻¹	km s ⁻¹
56889.4646	-26.5262	0.0065	-7.332	0.192	-0.0931	-3.174	55864.3650	-10.3379	0.0824	-35.4887	0.0450	-1.4658	-0.1402
56902.4309	-32.6324	0.0066	3.573	0.306	-0.0599	0.564	56147.5270	-63.8632	0.0919	32.2578	0.0477	-0.8636	-0.1345
56904.5962	-32.6380	0.0068	3.440	0.262	-0.0374	0.397	56243.3282	-31.7329	0.0865	-3.9741	0.0537	2.5450	-0.4209
56920.3467	-24.4103	0.0091	-7.056	0.298	-0.0155	-0.519	56525.5154	0.3692	0.0969	-45.6023	0.0465	1.0037	0.0557
56923.3604	-21.5792	0.0065	-9.635	0.230	-0.0122	0.204	56619.4355	1.8052	0.0935	-47.2845	0.0460	1.1267	0.0166
56935.2629	-9.7364	0.0066	-21.840	0.228	-0.0949	1.920	56889.5626	-5.5758	0.0959	-40.7870	0.0533	-1.3766	0.4097
56964.2858	-4.2257	0.0065	-32.487	0.238	-0.0185	-2.383	56948.4278	-4.2284	0.0907	-41.3813	0.0477	-0.2277	0.0637
56967.3061	-6.4232	0.0070	-26.063	0.208	0.0216	1.429	57295.4350	-2.6845	0.0851	-44.2049	0.0434	-0.9645	0.0944
56967.3092	-6.4251	0.0071	-26.097	0.215	0.0221	1.393	57349.4319	-62.3715	0.0769	31.5028	0.0470	0.0517	-0.1680
57295.3939	-32.2195	0.0064	3.414	0.211	-0.0010	0.817	57352.3389	-55.3175	0.0961	22.9637	0.0478	0.0353	0.1415
57305.3573	-31.2242	0.0072	2.262	0.505	0.0715	0.743	57353.3302	-52.7521	0.0988	19.2277	0.0513	-0.4543	0.2287
57602.5316	-30.8107	0.0064	1.103	0.438	0.1578	-0.034	57359.3294	-30.7757	0.0860	-4.1477	0.0468	2.6916	0.4199
57622.5357*	-13.8302*	0.0065*	-18.162*	0.258*	0.0859*	0.608*	57602.5586	-64.2228	0.0716	32.2981	0.0446	-1.2929	-0.0069
57634.4922	-3.6052	0.0065	-32.376	0.214	0.0110	-1.581	57967.5325*	-17.3970*	0.0902*	-23.8904*	0.0532*	-0.7115*	1.6796*
57967.5013*	-17.9611*	0.0064*	-15.122*	0.263*	0.1778*	-1.282*	58087.4119	-2.5781	0.0867	-44.7935	0.0471	-0.8063	-0.5589
58041.2560	-0.1183	0.0063	-34.254	0.252	0.2328	0.352							

relative to those of the other. Second, even if the uncertainties lead to exact relative weights, the uncertainties inferred from the covariance matrix will be false in the same proportions as the measurement uncertainties. For this reason, the uncertainties in Table 3 are systematically corrected after each orbit computation, by using the F_2 estimator of the goodness-of-fit defined in Stuart & Ord (1994):

$$F_2 = \left(\frac{9\nu}{2}\right)^{1/2} \left[\left(\frac{\chi^2}{\nu}\right)^{1/3} + \frac{2}{9\nu} - 1 \right] \quad (1)$$

where ν is the number of degrees of freedom and χ^2 is the weighted sum of the squares of the differences between the predicted and the observed values, normalized with respect to their uncertainties. When the predicted values are obtained through a linear model, F_2 follows the normal distribution $\mathcal{N}(0, 1)$. When non-linear models are used, but when the errors are small in comparison to the measurements, as hereafter, the model is approximately linear around the solution, and F_2 follows also $\mathcal{N}(0, 1)$. Therefore, the χ^2 of an orbit calculated with ν degrees of freedom must be close to the value corresponding to $F_2=0$, which is:

$$\chi_0^2 = \nu \left(1 - \frac{2}{9\nu}\right)^3 \quad (2)$$

The correction of the RV uncertainties is done as explained hereafter: First, the components are treated separately. A noise ε is added quadratically to the RV uncertainties in order to have, for each component, an SB1 solution with $\chi^2 = \chi_0^2$. This gives the relative weights of the components in the calculation of the SB2 solution. The final uncertainties are derived by applying a multiplying factor, $\varphi = \sqrt{\chi^2/\chi_0^2}$, so that the SB2 solution satisfies the condition $F_2 = 0$. Thus, the corrected uncertainties are given by the equations 3 and 4 hereafter:

$$\sigma_{RV,1}^{\text{corr}} = \varphi_1 \times \sqrt{\sigma_{RV,1}^2 + \varepsilon_1^2} \quad (3)$$

$$\sigma_{RV,2}^{\text{corr}} = \varphi_2 \times \sqrt{\sigma_{RV,2}^2 + \varepsilon_2^2} \quad (4)$$

With the procedure described above, the coefficients φ_1 and φ_2 are necessarily equal. However, it sometimes happens that the TODMOR uncertainties of a component produce an SB1 orbit with a χ^2 smaller than χ_0^2 . In this case, the noise

ε is null and the uncertainties are multiplied by the factor $\sqrt{\chi^2/\chi_0^2}$, which contributes to the φ -factor of the component.

The correction terms of the RV uncertainties of the 10 SB2 are listed in Table 4. HIP 20601 is the only exception to the “ $\varphi_1 = \varphi_2$ ” rule, for the reason explained above.

The previously published RV measurements were also corrected. In most cases, the method was modified in order to maintain the relative weights of the measurements. For this purpose, corrections are based solely on multiplicative coefficients φ_1 and φ_2 . Since obtained through another process, these RVs are generally biased and they reduce the reliability of the other orbital parameters. Therefore, they are used only to recalculate the period: When the period from our measurements completed by previously published measurements is at least 4 times more accurate than that from our measurements alone, the orbital elements are derived from the SOPHIE RVs, setting the period to this new value.

The orbital elements of the 10 stars are presented in Table 5. They include the following parameters: the period, P , the periastron epoch, T_0 , the eccentricity, e , the systemic radial velocity, V_0 , the periastron longitude, ω_1 , the RV semi-amplitudes of both components, K_1 and K_2 , and the offset of the RVs of the secondary component from that of the primary component, d_{2-1} . When the previously published RV measurements were taken into account to derive the period, the offset of the SOPHIE RVs, d_{n-p} , is indicated. The table also includes the minimum masses, $\mathcal{M}_1 \sin^3 i$ and $\mathcal{M}_2 \sin^3 i$, and the minimum semi-major axes, $a_1 \sin i$ and $a_2 \sin i$, which are derived from the solution terms. The spectroscopic orbits are shown in Figure 1 and the residuals are in Figure 2.

Among the ten SB2s, HIP 20601 belongs to a multiple system, since Griffin et al. (1985) found a faint distant visual component. This star was observed by the Gaia satellite as Gaia DR2 3283823383389256064 (Gaia collaboration 2018). Its separation relative to HIP 20601 was 7.09 arcsec, well above the diameter of the fibre of the SOPHIE spectrometer, which is 3 arcsec. Although an observation of HIP 20601 by poor seeing observation could still be contaminated at such a distance, the low magnitude of this companion ($G = 12.97$ mag i.e. 4 magnitudes fainter than HIP 20601) makes such contamination perfectly negligible, as evidenced by the low residuals in the SB2 orbit, Figure 2.

5 MASSES AND PARALLAXES OF FIVE STARS RESOLVED BY INTERFEROMETRY

5.1 Calculation method

Of the ten SB2s, five were sufficiently observed by interferometry to calculate a combined orbit giving the masses of the components and the trigonometric parallax of the system. However, before combining RVs and interferometric measurements, uncertainties must first be corrected. This has been done for the RVs in Section 4, but remains to be done for interferometric measurements. The method is similar to that applied to RV uncertainties in Section 4: The visual orbit is calculated and the χ^2 is considered. From this we deduce the corrective coefficient that must be applied to

the uncertainties for $F_2 = 0$. After this correction, the combined spectroscopic and interferometric orbit is derived from the RVs and from the relative positions. The solution terms are P , T_0 , e , V_0 , ω_1 , and d_{2-1} as for the SB2 orbits, but also the position angle of the ascending node, Ω , the inclination of the orbital plane, i , the masses of the components, \mathcal{M}_1 and \mathcal{M}_2 , and the trigonometric parallax of the binary star, ϖ . The apparent semi-major axis, a , is finally derived from P , \mathcal{M}_1 , \mathcal{M}_2 and ϖ .

The uncertainties of the solution terms are extracted from the variance-covariance matrix of the Levenberg–Marquardt calculation, but the uncertainty of a is estimated by simulations, as explained hereafter: The solution terms that we have derived are used to calculate the RVs or the relative position for each observation epoch. Simulated measurements are produced by adding, to these model values, errors generated according to the $\mathcal{N}(0, \sigma_0)$ distribution, where σ_0 is the measurement uncertainty we finally obtained. A value of a is then calculated from the set of simulated measurements. The uncertainty of a is the standard deviation of the values thus obtained.

The simulation program was also used to verify that the uncertainty correction process presented above and in Section 4 does not introduce an error that would add to the uncertainties estimated from the Levenberg–Marquardt calculation. We have implemented the correction of the uncertainties of the simulated measurements by a multiplicative coefficient in order to have a zero χ^2 after the calculation of the SB1 orbit of each component, then the SB2 orbit, as well as the interferometric orbit. It thus appeared that the standard deviations of the solution terms calculated in the simulations were not affected by this modification, and remained equal to the uncertainties we had found. Although the uncertainty correction implemented in the simulation is slightly simpler than that applied to real measurements, this shows the robustness of the correction process. The simulations also allowed us to verify the absence of anomalies in the correlations between the different orbital parameters.

The results obtained for the five binaries are presented in Table 6. In this table, the standard deviation of the astrometric residuals of the combined solution is followed by the standard deviation of the astrometric-only solution, in parentheses. A comparison between these two terms shows that they are quite close, and such a similarity also appears if one compares the standard deviations of the radial velocities, $\sigma_{(o-c) RV}$, with the values in Table 5. This resemblance reflects the compatibility between the astrometric and spectroscopic contributions of the combined solution.

5.2 HIP 20601

The interferometric measurements we obtained for this star have been published in Table 1 of Paper II, where the uncertainties were corrected so that the visual orbit had $F_2 = 0$. Unlike Paper II, the spectroscopic part now consists only of our SOPHIE observations, with the reduction by TODMOR seen above, which ensures much more reliable results. The parameters of the combined orbit are in Table 6. The masses of the components are determined with a remarkable accuracy of 0.19% and 0.13% (about twice better than in Paper II). The orbit remains visually very close to that shown in Figure 1 of Paper II, and it is useless to reproduce it here.

Table 4. Correction terms applied to the uncertainties of the previous and of the new RV measurements. The composition of these terms into a uncertainty correction is set out in Section 4, eqs. 3 and 4. When the original publication provides only weights for the previous measurements, $\varphi_{1,p}$ and $\varphi_{2,p}$ are the uncertainties corresponding to $W = 1$, for the primary and for the secondary component, respectively.

HIP	#	Reference of previous RV	Correction terms for previous measurements				Correction terms for new measurements			
			$\varepsilon_{1,p}$ km s ⁻¹	$\varphi_{1,p}$	$\varepsilon_{2,p}$ km s ⁻¹	$\varphi_{2,p}$	$\varepsilon_{1,n}$ km s ⁻¹	$\varphi_{1,n}$	$\varepsilon_{2,n}$ km s ⁻¹	$\varphi_{2,n}$
HIP	7134	Griffin & Emerson (1975)	0	0.931	0.0123	1.009	0.1617	1.009
HIP	20601	Griffin et al. (1985) ^a	0	0.807	0.1052	1.029
HIP	61732	Halbwachs, Mayor & Udry (2012) ^a	0.0357	1.292	0.	1.292
HIP	73449	Goldberg et al. (2002) ^b	0	0.898	0	0.714	0.0898	0.961	0.1183	0.961
HIP	76006	Griffin (2005) ^c	0	0.300	0	1.147	0.0693	1.049	0.2621	1.049
HIP	77725	Tokovinin et al. (2000) ^a	0.1277	1.116	0.0742	1.116
HIP	96656	Balega et al. (2007) ^a	0.0060	1.255	0.0363	1.255
HIP	101452	no RV published	0	0.491	0.8295	0.877
HIP	104987	Massarotti et al. (2008)	0	0.605	0	1.532	0.1167	0.857	2.0016	0.857
HIP	117186	Nordström et al. (1997)	0	1.837	0	1.487	1.0851	1.203	0.2761	1.203

^a The previous measurements don't improve the accuracy of the period, and they were not taken into account.

^b The components were swapped before calculating the uncertainties.

^c the radial velocities of the blend have been taken into account by assigning them an uncertainty of 0.340 km s⁻¹.

The trigonometric parallax is 4.6 σ larger than that found in the second *Gaia* DR (DR2), which is (17.32 ± 0.13) mas. The difference is probably due to the orbital motion, which was ignored in the reduction of the *Gaia* DR2. In addition, we note that our uncertainty is 3.8 times smaller than that of *Gaia* DR2.

5.3 HIP 77725

This star is the visual binary BAG 7 and the Sixth Catalogue of Orbits of Visual Binary Stars³ mentions a combined visual and spectroscopic orbit by Tokovinin et al. (2000).

We found several interferometric measurements in the INT4 catalogue, and we selected the 11 of them that had measurement uncertainties. A component inversion was corrected for the observation of 2008.4717, and we put the measurements in the same format as the PIONIER measurements: times in years were converted to Julian days, and the uncertainties on θ and ρ were converted into uncertainty ellipsoids aligned with the apparent separation, ρ .

A first calculation of the visual orbit then gives a solution with $F_2 = 4.82$. The uncertainties σ_a and σ_b were therefore corrected by multiplying them by 2.016 to obtain a visual orbit of $F_2 = 0$. The positions thus transformed and the final uncertainties are in Table 7.

The combined orbit was derived, and the solution terms in Table 6 were obtained. The interferometric orbit and the residuals are shown in Figure 3. The masses of the components are slightly different but much more accurate than those derived by Tokovinin et al. (2000), which were $\mathcal{M}_1 = (0.48 \pm 0.13) \mathcal{M}_\odot$ and $\mathcal{M}_2 = (0.46 \pm 0.12) \mathcal{M}_\odot$. The *Gaia* DR2 gives the trigonometric parallax $\varpi = 47.29 \pm 0.17$ mas, which is 4.4 σ smaller than our result. Again, the difference may be due to the orbital motion.

5.4 HIP 96656

This star is the nearby star GJ 765.2, and the double star MLR 224. Balega et al. (2007) observed it with the 6m “large altazimuth telescope” (Russian: Bolshoi Teleskop Altazimutalnyi, or BTA6), and obtained high-precision speckle measurements. They also took over visual measurements of lower quality, and combined all these measurements with radial velocities measured with spectrovelocimeters. They thus determined the masses of the components with an accuracy of 2.4 to 2.5 %.

We have ignored the visual measurements because of their poor quality, but have taken the BTA6 speckle measurements. As for HIP 77725, the epoch in years were converted in Julian days, and the parameters of the error ellipsoid, σ_a , σ_b and θ_a , were derived from the position angle θ and from the uncertainties on θ and ρ given in Section 2 of the paper by Balega et al.; the uncertainties were increased by 2.4 % in order to obtain a visual orbit with $F_2 = 0$. The measurement in Table 8 were thus obtained. By combining the speckle measurements and our radial velocities, we found a combined orbit including the visual part presented in Figure 4. The elements are in Table 6. The mass accuracy is now 0.45 % for the primary component and 0.29 % for the secondary, 5 and 8 times better than in Balega et al., respectively.

The parallax of the combined solution is 31.26 ± 0.11 mas, in disagreement with the 33.67 ± 0.53 mas given by the *Gaia* DR2. Again, the difference probably comes from the orbital motion, neglected in the *Gaia* reduction.

5.5 HIP 104987

The INT4 catalogue contains many observations of this star, including a series of 29 measurements from the Mark III Optical Interferometer published by Armstrong et al. (1992). These measurements are individually less accurate than PIONIER measurements, but their number still improves the accuracy of orbital parameters. We have therefore added them to our own measures, as follows:

- The uncertainties of each set of measurements are cor-

³ <https://www.usno.navy.mil/USNO/astrometry/optical-IR-prod/wds/orb6>

Table 5. The orbital elements of the SB2s. The radial velocity of the barycentre, V_0 , is in the reference system of the new measurements of the primary component. The minimum masses and minimum semi-major axes are derived from the true period ($P_{true} = P \times (1 - V_0/c)$). The numbers in parentheses refer to the previously published RV measurements that were taken into account, in addition to the new ones, to derive the period, P ; the other elements correspond to the new RVs alone.

HIP HD/BD	#	P (d)	T_0 (BJD) 2400000+	e	V_0 (km s ⁻¹)	ω_1 ($^\circ$)	K_1 K_2 (km s ⁻¹)	$\mathcal{M}_1 \sin^3 i$ $\mathcal{M}_2 \sin^3 i$ (\mathcal{M}_\odot)	$a_1 \sin i$ $a_2 \sin i$ (Gm)	N_1 N_2	d_{n-p} d_{2-1} (km s ⁻¹)	$\sigma(O_1 - C_1)$ $\sigma(O_2 - C_2)$ (km s ⁻¹)
HIP HD	7134 9313	53.51164 ± 0.00012	55008.0873 ± 0.0044	0.39674 ± 0.00027	-15.1227 ± 0.0038	279.717 ± 0.037	24.6998 ± 0.0058 34.674 ± 0.075	0.5242 ± 0.0025 0.37342 ± 0.00096	16.6843 ± 0.0037 23.422 ± 0.051	16 16	0.4981 ± 0.0528	0.011 0.201
HIP HD	20601 27935	156.380540 ± 0.000095	56636.67055 ± 0.00046	0.851280 ± 0.000031	41.5967 ± 0.0041	201.984 ± 0.015	37.3352 ± 0.0031 50.322 ± 0.040	0.9050 ± 0.0016 0.67143 ± 0.00065	42.1207 ± 0.0056 56.772 ± 0.045	16 16	0.1544 ± 0.0509	0.0080 0.131
HIP BD	61732 +17 2512	595.18 ± 0.20	57210.58 ± 0.87	0.3393 ± 0.0019	-15.956 ± 0.032	64.85 ± 0.67	9.197 ± 0.021 13.068 ± 0.034	0.3326 ± 0.0022 0.2341 ± 0.0014	70.81 ± 0.17 100.61 ± 0.27	11 11	0.3466 ± 0.0736	0.043 0.084
HIP HD	73449 ^a 132756	2528.6 ± 1.0	57708.5 ± 4.0	0.3752 ± 0.0023	8.147 ± 0.038	99.54 ± 0.74	10.175 ± 0.048 10.253 ± 0.037	0.8928 ± 0.0080 0.8861 ± 0.0092	327.9 ± 1.5 330.4 ± 1.2	11 (45) 11 (45)	0.3868 ± 0.1434 0.0041 ± 0.0515	0.097 (0.862) 0.069 (0.758)
HIP HD	76006 ^a 138525	581.816 ± 0.025	56717.21 ± 0.23	0.6460 ± 0.0033	-47.331 ± 0.031	134.51 ± 0.51	13.640 ± 0.048 16.47 ± 0.11	0.4004 ± 0.0052 0.3316 ± 0.0027	83.31 ± 0.18 100.60 ± 0.61	12 (51) 12 (51,15 ^b)	-0.9549 ± 0.0521 0.4104 ± 0.1039	0.052 (0.310) 0.264 (1.317 ^b)
HIP BD	77725 +11 2874	1016.2 ± 1.2	56911.2 ± 2.3	0.3459 ± 0.0063	-0.335 ± 0.049	329.0 ± 1.3	6.749 ± 0.061 6.780 ± 0.044	0.1079 ± 0.0016 0.1074 ± 0.0020	88.49 ± 0.75 88.90 ± 0.50	13 13	-0.1453 ± 0.0722	0.135 0.070
HIP HD	96656 186922	4350.0 ± 2.2	57737.8 ± 2.7	0.24294 ± 0.00066	-3.2920 ± 0.0061	70.03 ± 0.26	7.3500 ± 0.0049 8.062 ± 0.017	0.7879 ± 0.0035 0.7183 ± 0.0020	426.49 ± 0.35 467.8 ± 1.0	14 14	0.1267 ± 0.0176	0.008 0.053
HIP HD	101452 196133	87.6834 ± 0.0020	57097.926 ± 0.049	0.6806 ± 0.0013	-7.608 ± 0.058	243.39 ± 0.14	35.272 ± 0.045 51.08 ± 0.34	1.361 ± 0.020 0.9396 ± 0.0080	31.158 ± 0.039 45.12 ± 0.30	11 11	0.0295 ± 0.3153	0.050 0.772
HIP HD	104987 ^a 202447/8	98.8051 ± 0.0023	57249.523 ± 0.042	0 ^c (fixed)	-16.445 ± 0.027	0 ^c (fixed)	16.190 ± 0.036 18.92 ± 0.61	0.239 ± 0.016 0.2043 ± 0.0071	21.998 ± 0.049 25.70 ± 0.82	14 (108) 14 (108)	-0.2766 ± 0.0678 0.6472 ± 0.4715	0.088 (0.645) 1.470 (1.503)
HIP HD	117186 ^a 202447/8	85.8244 ± 0.0013	56402.66 ± 0.15	0.3339 ± 0.0043	-21.03 ± 0.39	176.78 ± 0.67	32.59 ± 0.47 40.79 ± 0.14	1.636 ± 0.026 1.307 ± 0.037	36.26 ± 0.52 45.38 ± 0.18	14 (19) 14 (19)	-0.3657 ± 0.5651 0.9052 ± 0.4392	1.367 (1.980) 0.276 (1.175)

^a The elements were derived fixing P to the value obtained taking also the previous measurements into account.

^b Fifteen blend measurements were taken into account, with $\sigma(O - C) = 0.342$ km s⁻¹.

^c We have assumed a circular orbit since our RVs give the eccentricity $e = 0.00000002 \pm 0.0022$.

rected as explained in Section 5.1, by calculating the interferometric orbit with each of them. A correction coefficient of 0.6086 is thus found for the uncertainties of the Armstrong's measurements, and a coefficient of 0.1626 for ours.

- A comparison between the orbital elements from Armstrong et al. and those from PIONIER shows that the components have been inverted. Since PIONIER's position angles are compatible with the spectroscopic orbit, we correct the position angles of Armstrong et al. by 180 degrees.

- The interferometric orbit is derived again from the two sets together. The F_2 estimator of the orbit is 1.03, inferring an acceptable compatibility between the two sets. An addi-

tional correction of 1.0856 is still applied in order to have $F_2 = 0$.

The measurements with corrected uncertainties are presented in Table 9. They were used to derive the combined spectroscopic and interferometric solution which is presented in Table 6, and in Figure 5.

The eccentricity of the orbit is very small for a binary with a period of nearly 100 days, and this is probably due to the evolution of the primary component to the current G6 IV type. Our results provide a relevant insight into the achievement of the circularization of the orbit: The SB2 solution given in Table 5 is circular since the calculation

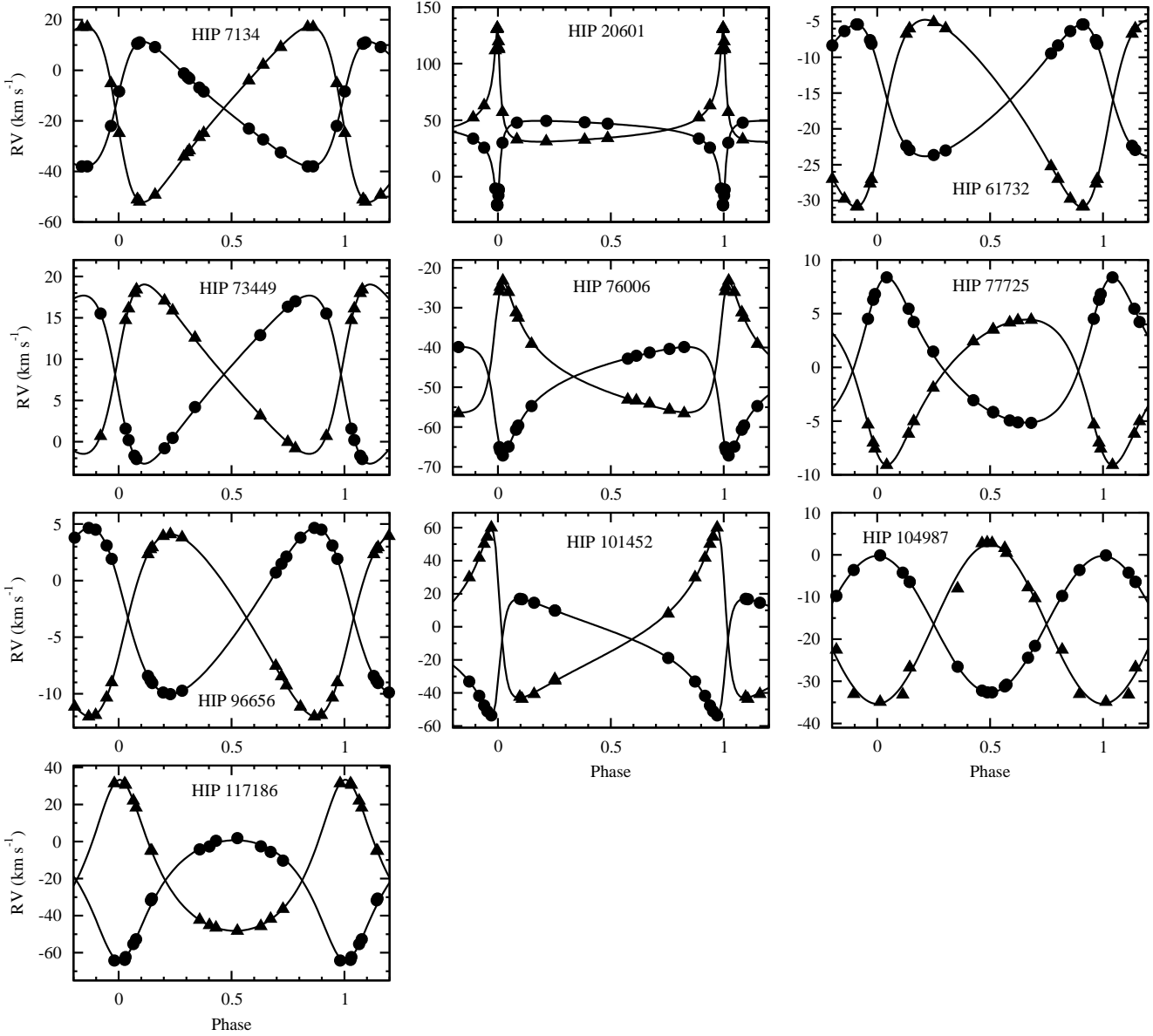


Figure 1. The spectroscopic orbits of the 10 SB2; the circles refer to the primary component, and the triangles to the secondary. For each SB2, the RVs are shifted to the zero point of the SOPHIE measurements of the primary component.

of an eccentric orbit lead to an eccentricity that is clearly not significant, with $e/\sigma_e = 1.8 \cdot 10^{-8} \pm 2.24 \cdot 10^{-3}$; this is in agreement with Eggleton & Yakut (2017), who assumed that the orbit is circular. On the other hand, the eccentricity of the interferometric orbit is $(4.76 \pm 0.82) \cdot 10^{-3}$. This value is significant, compatible at the 2σ -level with the value of the SB2 solution, and we observe that the interferometric measurements from the INT4 catalogue give nearly the same periastron longitude as the PIONIER measurements: $\omega = (283.8 \pm 8.3)^\circ$ for the former and $\omega = (288 \pm 17)^\circ$ for the latter. Therefore, we conclude that the orbit of HIP 104987 is not perfectly circular, and we adopt the eccentricity of the combined orbit, that is in Table 6; this value is significant at the 5.5σ -level.

The masses we found are compatible with those of Eggleton & Yakut (2017), which are respectively 2.000 and 1.847 solar masses.

This star is not included in the *Gaia* DR2, but the parallax provided by the *Hipparcos 2* catalogue (van Leeuwen 2007) is (17.14 ± 0.21) mas, which is 3.0σ less than our result. The difference may be due to an underestimation of the Hipparcos uncertainty.

5.6 HIP 117186

As well as HIP 20601 and HIP 104987, this star was observed by interferometry with the PIONIER instrument. Its measurements were presented in Paper II. By combining them with the RVs of this star, we have obtained the elements shown in Table 6. These are not really different from the preliminary elements given in Paper II, but they are more reliable, due to the better quality and homogeneity of the RVs.

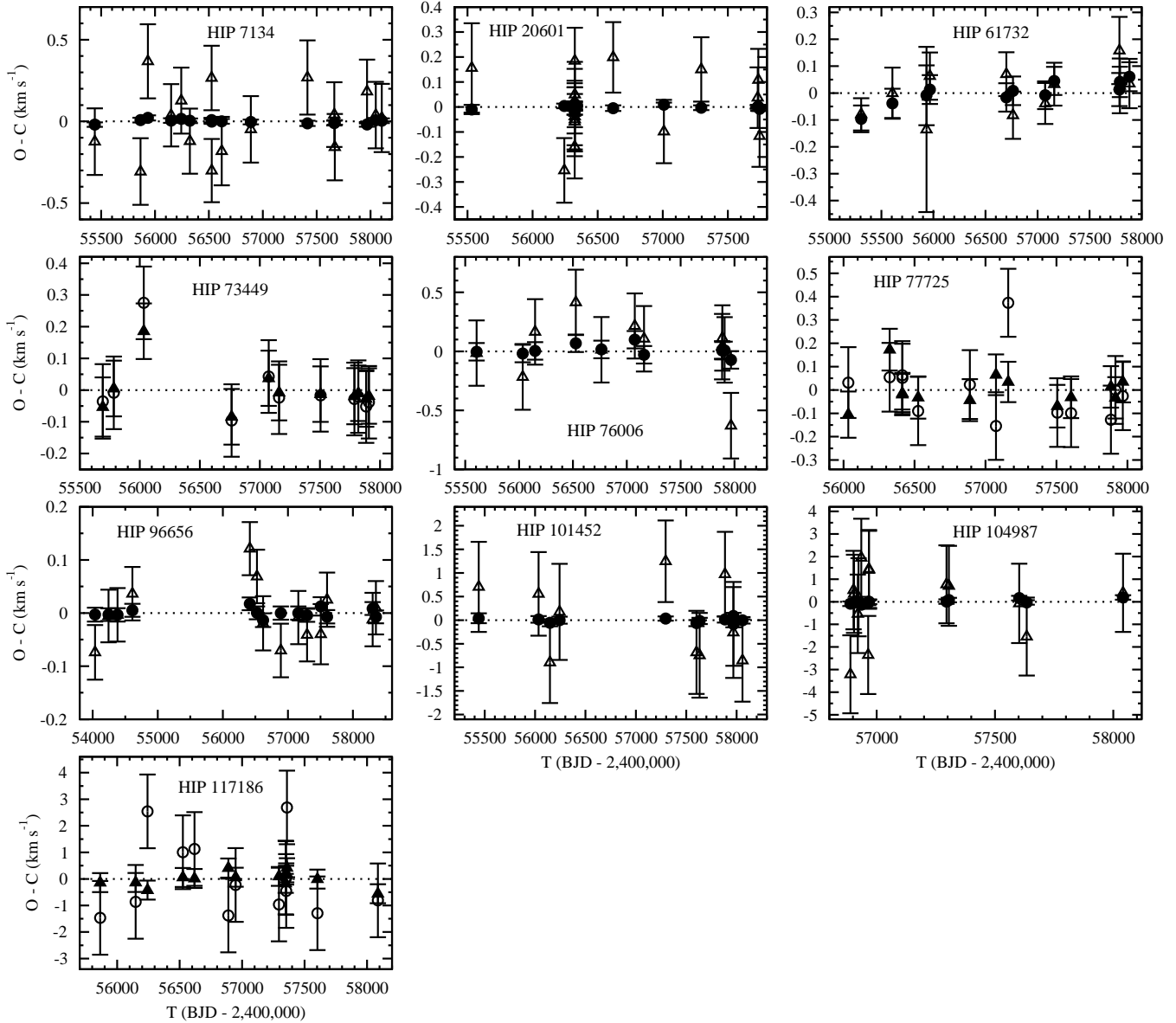


Figure 2. The residuals of the RVs obtained from TODMOR for the 10 SB2s. The circles refer to the primary component, and the triangles to the secondary component. For readability, the residuals of the most accurate RV measurements are in filled symbols.

The parallax is 3.7σ larger than that found in the *Gaia* DR2, which is (8.215 ± 0.044) mas.

5.7 Hertzsprung-Russell diagram and mass-luminosity relation

Figure 6 shows the location in the Hertzsprung-Russell (hereafter HR) diagram of the ten stars in the five SB2 systems for which we have inferred the individual masses, while Figure 7 shows their position in the mass-luminosity plane.

To draw these figures, we started from the effective temperatures, metallicities, and surface gravities given in Table 2. We corrected the metallicity by adding $+0.12$ to each $[\text{Fe}/\text{H}]$ -value to account for the fact that in our study the solar spectrum is adjusted with $[\text{Fe}/\text{H}]_{\odot} = -0.12$ (as specified in the table caption). Following the conservative guidelines given in the footnotes of Table 2, we added quadratically a

systematic error of 100 K on the effective temperature and 0.10 on $[\text{Fe}/\text{H}]$.

For two systems, HIP 20601 and HIP 117186, the spectroscopic values in Table 2 differ from values in the literature. HIP 20601 is a probable member of the Hyades open cluster. Our corrected value of the metallicity ($[\text{Fe}/\text{H}] = -0.05 \pm 0.13$) differs by 2σ from the recent determination of the cluster average metallicity by Dutra-Ferreira et al. (2016), $[\text{Fe}/\text{H}] = 0.18 \pm 0.03$ which is a robust value. If we fix the metallicity to this latter value and optimize again all other parameters, we get $T_{\text{eff,A}} = 6100 \pm 180$ K, $T_{\text{eff,B}} = 4600 \pm 90$ K, $\log g_A = 4.9 \pm 0.2$, $\log g_B = 5.2 \pm 0.2$, and unchanged $V \sin i$'s and flux ratio. As for HIP 117186, we noticed that the effective temperature of the A-component ($T_{\text{eff,A}} = 6208 \pm 138$ K) in Table 2 is smaller by more than 600 K than the value derived by Casagrande et al. (2011) by photometric calibra-

Table 6. The combined VB+SB2 solutions. For consistency with the SB orbits and with the forthcoming astrometric orbit, ω refer to the motion of the primary component. Except for HIP 77725 and HIP 96656, ΔH comes from the flux ratios deduced from the PIONIER observations. The standard deviation of the astrometric residuals $\sigma_{(o-c) VB}$ in parentheses refers to the astrometric-only solution.

	HIP 20601	HIP 77725	HIP 96656	HIP 104987	HIP 117186
P (days)	156.380534 ± 0.000094	1015.53 ± 0.55	4345.3 ± 1.4	98.80450 ± 0.00035	85.8364 ± 0.0064
T_0 (BJD-2400000)	56636.67052 ± 0.00046	56904.5 ± 1.6	57739.1 ± 2.0	57277.7 ± 1.7	56402.368 ± 0.094
e	0.851282 ± 0.000031	0.3415 ± 0.0017	0.24280 ± 0.00065	0.00417 ± 0.00076	0.32778 ± 0.00073
V_0 (km s $^{-1}$)	41.5968 ± 0.0041	-0.356 ± 0.043	-3.2884 ± 0.0053	-16.458 ± 0.027	-21.11 ± 0.36
ω_1 ($^\circ$)	201.983 ± 0.015	325.51 ± 0.81	70.18 ± 0.20	102.9 ± 6.3	175.50 ± 0.34
Ω ($^\circ$; eq. 2000)	340.513 ± 0.055	120.07 ± 0.50	292.78 ± 0.16	216.57 ± 0.16	16.942 ± 0.047
i ($^\circ$)	103.133 ± 0.072	36.49 ± 0.76	80.377 ± 0.097	151.52 ± 0.28	88.047 ± 0.043
a (mas)	11.338 ± 0.022	105.59 ± 0.73	189.38 ± 0.63	12.105 ± 0.013	4.677 ± 0.034
\mathcal{M}_1 (\mathcal{M}_\odot)	0.9798 ± 0.0019	0.510 ± 0.029	0.8216 ± 0.0037	2.20 ± 0.16	1.647 ± 0.022
\mathcal{M}_2 (\mathcal{M}_\odot)	0.72697 ± 0.00094	0.508 ± 0.029	0.7491 ± 0.0022	1.883 ± 0.083	1.316 ± 0.034
ϖ (mas)	16.703 ± 0.034	53.1 ± 1.3	31.26 ± 0.11	18.11 ± 0.24	8.551 ± 0.080
H (mag)	7.209 ± 0.047	8.489 ± 0.010	5.980 ± 0.023	2.442 ± 0.196	6.252 ± 0.031
ΔH (mag)	0.9990 ± 0.0158	$0.06^a \pm 0.02^a$	0.44 ± 0.24^b	2.1303 ± 0.0286	0.8914 ± 0.0074
d_{2-1} (km s $^{-1}$)	0.154 ± 0.050	-0.104 ± 0.053	0.119 ± 0.016	0.676 ± 0.471	1.067 ± 0.374
$\sigma_{(o-c) VB}$ (mas)	0.031 (0.024)	3.95 (3.75)	2.06 (2.07)	0.652 (0.665)	0.0080 (0.0081)
$\sigma_{(o-c) RV}$ (km s $^{-1}$)	0.0081, 0.131	0.116, 0.124	0.012, 0.050	0.090, 1.488	1.521, 0.298

^a according to Horch et al. (2017).^b from the data of Balega et al. (2007).**Table 7.** The interferometric measurements of HIP 77725, taken from the INT4 catalogue and adapted to our purpose. ρ is the apparent separation and θ is the position angle of the secondary component. σ_a and σ_b are the semi-major axis and the semi-minor axis of the ellipsoid error, respectively; they are derived as explained in the text. θ_a is the position angle of the major axis of the ellipsoid error. The position angles are all given for the equinox of the observation epoch.

$T-2,400,000$ (BJD)	ρ (mas)	θ ($^\circ$)	σ_a (mas)	σ_b (mas)	θ_a ($^\circ$)
49115.344	109.0	56.4	7.66	6.04	146.4
49116.257	103.0	56.2	7.24	6.04	146.2
50178.528	115.3	68.4	4.05	4.03	158.4
50591.726	102.0	135.7	7.17	6.04	45.7
52393.977	132.0	101.9	4.03	2.78	101.9
53898.921	68.0	293.5	4.03	3.11	113.5
54638.756	107.0	140.4	6.04	4.89	140.4
56725.859	90.9	156.2	1.21	0.638	156.2
57085.842	84.8	5.0	0.298	0.201	95.0
57220.616	103.8	50.9	1.21	1.09	50.9
57220.616	103.4	51.7	0.727	0.604	141.7

tion ($T_{\text{eff,A}} = 6853 \pm 80$ K), while Casagrande et al.'s metallicity ($[\text{Fe}/\text{H}] = 0.11 \pm 0.10$) is higher than our corrected value, although still within the error bars. If we take Casagrande et al.'s metallicity as a robust value and optimize again, we get $T_{\text{eff,A}} = 7200 \pm 30$ K, $T_{\text{eff,B}} = 7150 \pm 70$ K, $\log g_A = 3.8 \pm 0.2$, $\log g_B = 4.1 \pm 0.2$. In the following, we adopt these latter sets of parameters for the two couples.

To derive the individual luminosities, we proceeded in two steps. We first derived the individual apparent magnitudes from the magnitude difference between the components of HIP 20601, HIP 96656, HIP 104987, and HIP 117186 measured in the H -band by PIONIER. For HIP 77725, we used the magnitude difference in infrared measured by Horch et al. (2017) with the WYIN telescope.

Table 8. The interferometric measurements of HIP 96656, taken from Balega et al. (2007) and adapted to our purpose. ρ is the apparent separation and θ is the position angle of the secondary component. σ_a and σ_b are the semi-major axis and the semi-minor axis of the ellipsoid error, respectively; they are derived as explained in the text. θ_a is the position angle of the major axis of the ellipsoid error. The position angles are all given for the equinox of the observation epoch.

$T-2,400,000$ (BJD)	ρ (mas)	θ ($^\circ$)	σ_a (mas)	σ_b (mas)	θ_a ($^\circ$)
49116.111	35.0	151.7	4.08	1.87	151.7
49296.029	52.0	264.7	4.08	2.78	84.7
49613.425	129.0	285.1	1.53	1.15	105.1
50736.983	165.7	303.3	1.53	1.47	123.3
50736.983	165.9	303.0	1.53	1.48	123.0
51097.842	111.0	311.3	1.53	0.988	131.3
51476.160	46.0	348.3	1.53	0.409	168.3
51865.253	68.0	80.8	1.53	0.605	80.8
52184.474	122.0	99.3	1.53	1.09	99.3
52215.483	128.0	100.2	1.53	1.14	100.2
52567.577	165.0	108.3	1.76	1.70	108.3
52567.577	165.0	107.8	1.76	1.70	107.8
52567.577	163.0	107.9	1.76	1.68	107.9
52567.577	163.0	107.8	1.76	1.68	107.8
53303.175	82.0	126.8	1.53	0.730	126.8
53895.963	115.0	282.6	1.53	1.02	102.6

Then, we calculated the luminosities from the apparent magnitudes, the trigonometric parallaxes of Table 6, and the bolometric corrections of Casagrande & VandenBerg (2018), the latter being functions of the effective temperature, metallicity, and surface gravity.

In Figures 6 and 7, we show the position of several stellar evolutionary tracks and isochrones taken from the updated BaSTI database (Hidalgo et al. 2018). These models include state-of-the-art input physics and add overshooting of convective cores on the main sequence. As indicated on

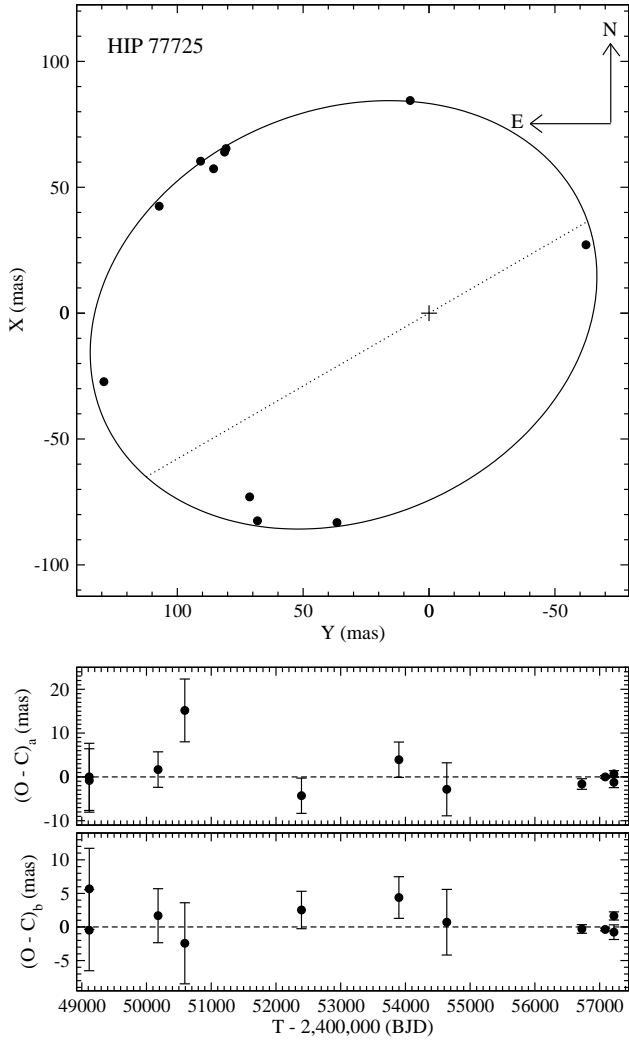


Figure 3. The visual part of the combined orbit of HIP 77725. Upper panel: the visual orbit; the circles are the positions from Table 7; the node line is in dashes. Middle panel: the residuals along the semi-major axis of the error ellipsoid. Lower panel: the residuals along the semi-minor axis of the error ellipsoid.

the figure, the evolutionary tracks correspond to the range of metallicities and masses of the studied SB2 members, while the isochrones fit the position of some of the stars. We now discuss the figure for each SB2 couple:

- HIP 20601. Due to their rather low mass, the stars are located in a region of the HR diagram where the evolution proceeds quite slowly. Therefore, they cannot be age-dated in this diagram. Since the system is a member of the Hyades cluster, we can assume that like the Hyades, it is aged $\sim 600 - 700$ Myr (Lebreton, Fernandes & Lejeune 2001). Indeed, we can see in the mass-luminosity plane (Fig. 7) that both components can be put on an isochrone of 700 Myr corresponding to the Hyades metallicity.

- HIP 77725. The stars have very similar masses. Due to their low mass, they are located in a region of the HR diagram where the evolution proceeds very slowly. Therefore their age is mostly undetermined. We notice that while their effective temperatures as derived in this study appear to be too hot with respect to those expected from the models,

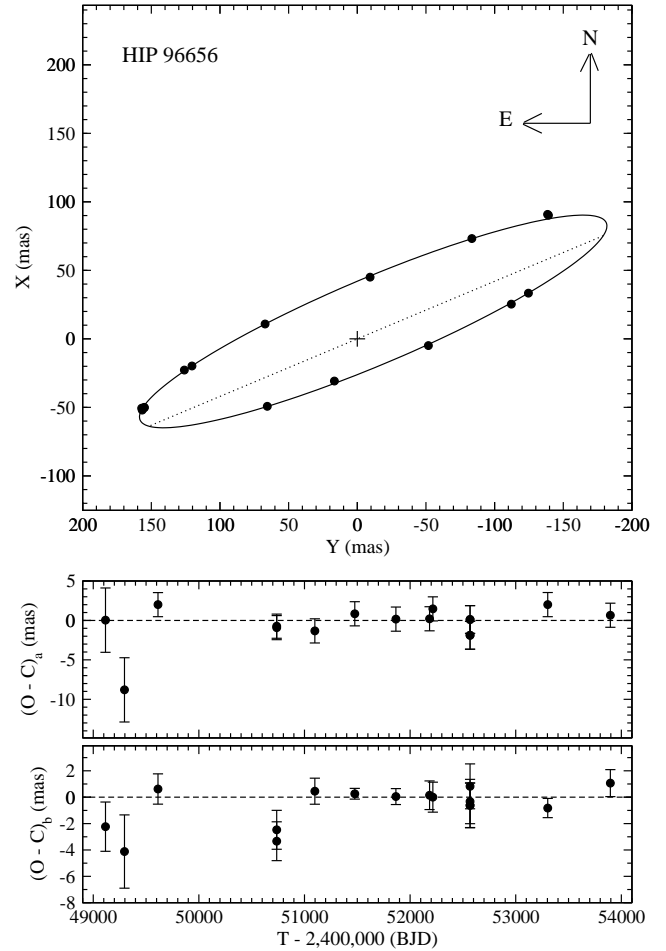


Figure 4. The visual part of the combined orbit of HIP 96656. Upper panel: the visual orbit; the circles are the positions from Table 8; the node line is in dashes. Middle panel: the residuals along the semi-major axis of the error ellipsoid. Lower panel: the residuals along the semi-minor axis of the error ellipsoid.

the stars reasonably fit in the theoretical mass-luminosity relation.

- HIP 96656. Again, the components have low mass and evolve slowly. In Fig. 6 the position of the components are well-fitted on the zero age main sequence at their metallicity, however the system cannot be age-dated accurately. Also, we note that both stars well fit in the theoretical mass-luminosity relation corresponding to their metallicity.

- HIP 104987. The two components can be positioned on isochrones of ages in the range $\approx 1000 - 1200$ Myr (the isochrone plotted is of 1100 Myr). This age is older than the age estimated by Griffin & Griffin (2002) which is not surprising since both the observed properties and stellar models have been considerably updated in the meantime. The system is evolved: according to BaSTI stellar models, the A-component lies close to the base of the red giant branch while the B-one is reaching the end of the main sequence. Both components sit on their isochrone in the theoretical mass-luminosity plane.

- HIP 117186. First, we point out that if we had taken the spectroscopic values of the effective temperatures and metallicity in Table 2, it would not have been possible to place the

Table 9. The interferometric measurements of HIP 104987. ρ is the apparent separation and θ is the position angle of the secondary component, defined as the lightest. σ_a and σ_b are the semi-major axis and the semi-minor axis of the ellipsoid error, respectively; they are corrected as explained in the text. θ_a is the position angle of the major axis of the ellipsoid error. The position angles are given for the equinox of the observation epoch. Observations dating back to before JD 2 450 000 come from Armstrong et al. (1992), after reversing the components. The others were carried out with the Auxiliary Telescopes of the ESO VLTI, using the PIONIER instrument.

$T-2,400,000$ (BJD)	ρ (mas)	θ ($^\circ$)	σ_a (mas)	σ_b (mas)	θ_a ($^\circ$)
47690.973	9.63	306.6	1.31	0.0540	90.9
47695.903	10.30	283.0	0.303	0.0270	104.5
47698.971	10.62	270.7	0.830	0.0607	90.8
47700.944	10.38	262.3	2.15	0.108	94.7
47715.955	12.39	213.8	2.59	0.385	80.6
47720.922	11.79	198.3	2.49	1.51	114.8
47746.781	10.25	96.7	1.69	0.324	106.5
47747.841	10.76	92.2	0.938	0.243	88.9
47751.822	11.33	78.0	0.668	0.121	88.6
47758.762	11.55	53.5	0.303	0.148	78.1
47761.720	11.62	41.5	0.762	0.148	108.2
47765.738	12.36	36.0	1.93	0.0674	99.4
47784.730	10.55	324.1	1.39	0.162	85.5
47813.730	11.21	209.6	2.77	1.11	74.4
47816.652	12.98	213.2	2.05	0.425	75.4
47817.639	11.28	201.8	0.938	0.256	77.9
47832.687	10.85	150.2	0.634	0.0607	69.9
47836.668	10.66	134.5	0.492	0.0540	76.1
48068.889	11.95	10.2	0.911	0.148	103.7
48070.934	13.01	342.0	3.18	0.499	93.2
48101.870	11.48	242.4	0.101	0.0270	86.4
48102.856	11.73	239.7	0.223	0.0540	88.8
48104.829	11.79	232.8	0.175	0.0338	94.9
48130.834	10.68	143.4	0.128	0.0270	82.4
48133.756	10.47	131.1	0.277	0.0472	86.3
48134.778	10.52	127.1	0.196	0.0338	85.8
48136.751	10.54	118.7	0.135	0.0338	96.2
48137.810	11.41	112.4	0.445	0.0540	81.4
48149.753	11.92	69.7	0.229	0.0540	81.4
56937.598	11.20	89.85	0.0600	0.0248	132.0
56939.599	11.37	82.22	0.0583	0.0229	135.0
56948.578	12.06	51.41	0.0724	0.0212	137.0
56949.537	12.09	48.49	0.0795	0.0530	147.0
56962.538	11.69	5.35	0.0707	0.0300	134.0
57537.870	11.73	63.44	0.0795	0.0406	172.0
57569.873	10.63	-50.42	0.1113	0.0883	119.0
57597.710	12.02	-151.36	0.0530	0.0300	4.0
57599.740	11.96	-158.26	0.0848	0.0335	15.0
57600.725	11.88	-161.20	0.1060	0.0459	147.0
57622.707	10.77	115.44	0.0741	0.0371	152.0
57625.659	10.88	103.52	0.0512	0.0318	3.0

stars on the same isochrone. On the other hand, with the revised T_{eff} based on the metallicity value of Casagrande et al. (2011), the components sit on an isochrone of 1500 Myr in the HR diagram as well as in the mass-luminosity plane.

We conclude that the properties of the SB2 couples are overall well retrieved by theoretical models in the mass-luminosity plane. Concerning the HR diagram, the fit is also

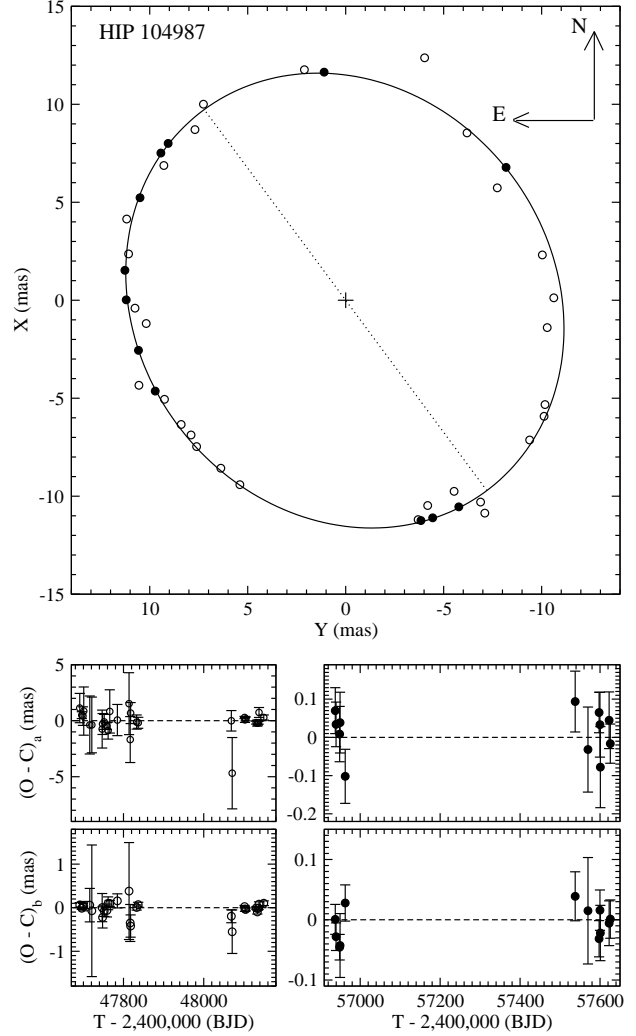


Figure 5. The visual part of the combined orbit of HIP 104987. Upper panel: the visual orbit; the circles are the positions from Table 9; open circles refer to the observations of Armstrong et al. (1992), while full circles represent our PIONIER measurements; the node line is in dashes. Middle panels: the residuals along the semi-major axis of the error ellipsoid; the observations of Armstrong et al. are in the left panel, and the PIONIER observations are in the right panel. Lower panels: the residuals along the semi-minor axis of the error ellipsoid.

satisfactory for the 5 systems, once the metallicity and, as a consequence, the effective temperatures of one of them (HIP 117186) have been revised after we adopted robust $[\text{Fe}/\text{H}]$ determination from the literature. The masses we determined in this study are very precise, while the characterization of the stars would benefit from further improvements in the determination of their luminosities, effective temperatures, and metallicities. The error bars on these latter are still too high to constrain the models. Furthermore, although very modern, stellar models are still being affected by uncertainties in their input physics and initial helium abundance. A full characterisation of the stars is well beyond the scope of the paper.

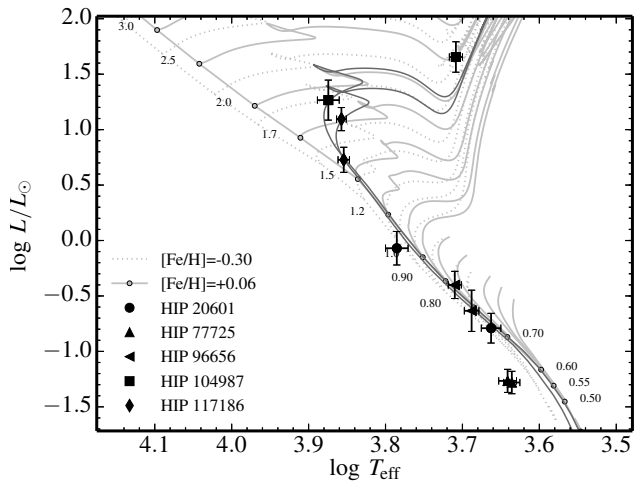


Figure 6. Hertzsprung-Russell diagram. The SB2 components are placed as well as stellar evolutionary tracks and isochrones taken in the BaSTI database (Hidalgo et al. 2018). Evolutionary tracks in the mass range 0.5 to $3.0 M_{\odot}$ are plotted in light grey for two values of the metallicity ($[\text{Fe}/\text{H}] = -0.30$ (dotted lines) and $+0.06$ (continuous lines)). In dark grey are plotted from top to bottom isochrones of 1100 Myr at metallicity $[\text{Fe}/\text{H}] = -0.03$ (HIP 104987) and 1500 Myr at metallicity $[\text{Fe}/\text{H}] = -0.11$ (HIP 117186).

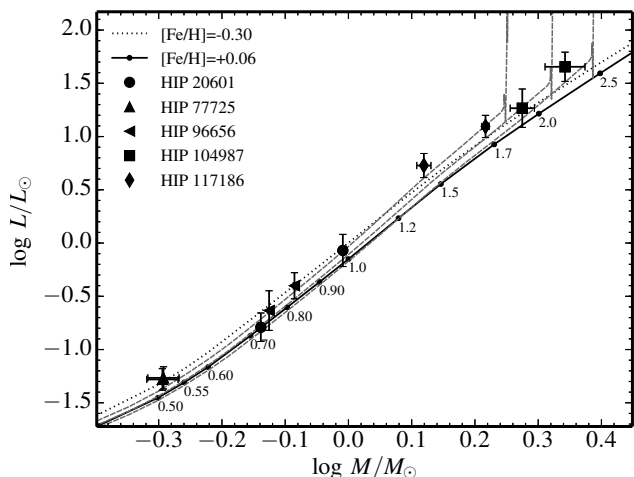


Figure 7. Mass-luminosity relation. The observed positions with error bars of the SB2 components are plotted. Black curves show the mass-luminosity relation on the zero age main sequence at two values of the metallicity, $[\text{Fe}/\text{H}] = -0.30$ (dotted line) and $+0.06$ (continuous line). Three isochrones are plotted with grey dashed lines. The isochrone at lower luminosities is for HIP 20601, that at higher luminosities for HIP 117186 and in-between is the one for HIP 104987, see text for details.

6 SUMMARY AND CONCLUSION

We have obtained 146 spectra for 10 SB2s: 7 SB2s previously known, and 3 binaries that were only SB1s. The RVs of the components were derived with the TODMOR cross-correlation algorithm. After discarding the RVs coming from 14 blended spectra, we have derived the orbital elements of the 10 SB2s.

We found minimal masses with an accuracy better than 1 % for 11 of the 20 components.

Five of the 10 SB2s have received enough long-baseline or speckle interferometric measurements to calculate the masses of their components. The PIONIER measurements of one of them, HIP 104987, were never published before. Thanks to these data, we have derived the masses of the components of these five binary stars with accuracies ranging from 0.13% to a few percents, and we have found that the orbit of HIP 104987 is not circular, although its eccentricity is very small. We were also able to provide an estimate of the state of evolution of these stars by placing them in the HR diagram.

Taking into account Paper III and IV, we have now accurate orbits for 34 SB2s, and combined SB2 and interferometric orbits for 9 of them. These latter will be useful to check the masses that will be obtained from *Gaia* in the future, and they can also be used to control the forthcoming DR3 parallaxes.

ACKNOWLEDGMENTS

This project was supported by the french INSU-CNRS “Programme National de Physique Stellaire”, and the Centre National des Etudes Spatiales (CNES). We are grateful to the staff of the Haute-Provence Observatory, and especially to Dr H. Le Coroller, Dr M. Véron, and the night assistants, for their kind assistance. PIONIER is funded by the Université Joseph Fourier (UJF), the Institut de Planétologie et d’Astrophysique de Grenoble (IPAG), and the Agence Nationale pour la Recherche (ANR-06-BLAN-0421, ANR-10-BLAN-0505, ANR-10-LABX56). The integrated optics beam combiner is the result of a collaboration between IPAG and CEA-LETI based on CNES R&T funding. We made use of the SIMBAD database, operated at CDS, Strasbourg, France.

REFERENCES

- Angelov T., 1996, BAbel, 154, 13
- Armstrong J.T., Mozurkewich D., Vivekanand M., Simon R.S., Denison C.S., et al., 1992, AJ 104, 241
- Balega Y.Y., Beuzit J.-L., Delfosse X., Forveille T., Perrier C., et al., 2007, A&A, 464, 635
- Bell E.F., de Jong R.S., 2001, ApJ 550, 212
- Berger J.-P., Zins G., Lazareff B., Le Bouquin J.-B., Jocou L., et al., 2010, Proc. SPIE, 7734, 35
- Casagrande L., Schönrich R., Asplund M., Cassisi S., Ramírez I., Meléndez J., Bensby T., Feltzing S., 2011, A&A, 530, A138
- Casagrande L., VandenBerg D. A., 2018, MNRAS, 479, L102
- Claret A., Torres G., 2019, ApJ 876, 134
- Dutra-Ferreira L., Pasquini L., Smiljanic R., Porto de Mello G. F., Steffen M., 2016, A&A, 585, A756, A&A, 585, A75
- Eggleton P.E., Yakut K., 2017, MNRAS 468, 3533
- Eker Z., Soydugan F., Soydugan E., Bilir S. et al., 2015, AJ 149, 131
- ESA, 1997, The Hipparcos and Tycho Catalogues, ESA SP-1200, vol. 10

- Gaia collaboration: Prusti T., de Bruijne J.H.J., Brown A.G.A., Vallenari A., Babusiaux C. et al., 2016, *A&A* 595, A1
- Gaia collaboration: Brown A.G.A., Vallenari A., Prusti T., de Bruijne J.H.J., Mignard F. et al., 2016b, *A&A* 595, A2
- Gaia collaboration: Brown A.G.A., Vallenari A., Prusti T., de Bruijne J.H.J., Babusiaux C. et al., 2018, *A&A* 616, A1
- Gallenne A., Pietrzyński G., Graczyk D., Pilecki B., Storm J. et al., 2019, *A&A* 632, A31
- Goldberg D., Mazeh T., Latham D.W., Stefanik R.P., Carney B.W., Laird J.B., 2002, *AJ*, 124, 1132
- Griffin R.E.M., Griffin R.F., 2002, *MNRAS* 330, 288
- Griffin R.F., 2005, *Observatory* 125, 367
- Griffin R.F., Emerson B., 1975, *Observatory* 95, 98
- Griffin R.F., Gunn J.E., Zimmerman B.A., Griffin R.E.M., 1985, *AJ* 90, 609
- Halbwachs J.-L., Mayor M., Udry S., 2012, *MNRAS* 422, 14
- Halbwachs J.-L., Arenou F., Pourbaix D., Famaey B., Guillout P. et al., 2014, *MNRAS* 445, 2371 (Paper I)
- Halbwachs J.-L., Boffin H.M.J., Le Bouquin J.-B., Kiefer F., Famaey B. et al., 2016, *MNRAS* 455, 3303 (Paper II)
- Hartkopf W.L., McAlister H.A., Mason B.D., 2001, *AJ* 122, 3480
- Hidalgo S. L., Pietrinferni A., Cassisi S., Salaris M., Mucciarelli A., Savino A., Aparicio A., Silva Aguirre V., Verma K., 2018, *ApJ*, 856, 125
- Hodgson R.M., Bailey D.G., Naylor M.J., Ng A.L.M., McNeil S.J., 1985, *Image Vision Comput.*, 3(1), 4-14
- Horch E. P., Casetti-Dinescu D. I., Camarata M. A., Bidarian A., van Altena W.F., et al., 2017, *AJ*, 153, 212
- Jancart S., Jorissen A., Babusiaux C., Pourbaix D., 2005, *A&A* 442, 365
- Kiefer, F., Halbwachs, J.-L., Arenou, F., Pourbaix, D., Famaey, B., et al., 2016, *MNRAS*, 458, 3272 (Paper III)
- Kiefer F., Halbwachs J.-L., Lebreton Y., Soubiran C., Arenou F., et al., 2018, *MNRAS*, 474, 731 (Paper IV)
- Le Bouquin J.B., Berger J.-P., Lazareff B., Zins G., Haguebauer P., et al., 2011, *A&A* 535, 67L
- Lebreton Y., Fernandes J., Lejeune T., 2001, *A&A*, 374, 540
- Lebreton Y., 2005, *The Three-Dimensional Universe with Gaia*, ESA SP-576, 493
- Lelli F., McGaugh S.S., Schombert J.M., 2016, *AJ* 152, 157
- Lester K.V., Gies D.R., Schaefer G.H., Farrington C.D., Monnier J.D. et al., 2019, *AJ* 157, 140
- McAlister H.A., 1996, *S&T* 92, 28
- Mann A.W., Dupuy T., Kraus A.L., Gaidos E., Ansdell M. et al., 2019, *ApJ* 871, 63
- Martin C., Mignard F., 1998, *A&A* 330, 585
- Massarotti A., Latham D.W., Stefanik R.P., Fogel J., 2008, *AJ*, 135, 209
- Moya A., Zuccarino F., Chaplin W.J., Davies G.R., 2018, *ApJSS* 237, 21
- Munari U., Dallaporta S., Siviero A., Soubiran C., Fiorucci M., Girard P., 2004, *A&A* 418, L31
- Nordström B., Stefanik R.P., Latham D.W., Andersen J., 1997, *A&ASS*, 126, 21
- Perruchot S., Kohler D., Bouchy F., Richaud Y., Richaud P., et al., 2008, *Proc. of the SPIE*, vol. 7014, 70140J
- Press, W.H., Teukolsky, S.A., Vetterling, W.T., Flannery, B.P., 1996, *Numerical Recipes in Fortran 90* (Cambridge University Press)
- Stuart A., Ord K., 1994, *Kendall's Advanced Theory of Statistics*, vol. 1. Edward Arnold, London
- Tokovinin A.A., Balega Y.Y., Hofmann K.H., Weigelt G., 2000, *Astron. Letters* 26, 668
- Torres G., Andersen J., Giménez A., 2010, *Astron. Astrophys. Rev.*, 18, 67
- Torres G., Sandberg C.H., Fekel F.C., Muterspaugh M.W., 2019, *ApJ* 876, 41
- van Leeuwen F., 2007, *A&A* 474, 653
- Zucker S., Mazeh, T., 1994, *ApJ*, 420, 806
- Zucker S., Mazeh T., Santos N. C., Udry S., Mayor M., 2004, *A&A*, 426, 695